

# Evolution of fault-surface roughness with slip

Amir Sagy

Emily E. Brodsky

Department of Earth and Planetary Sciences, University of California–Santa Cruz, Santa Cruz, California 95064, USA

Gary J. Axen

Department of Earth and Environmental Science, New Mexico Institute of Mining and Technology, Socorro, New Mexico 87801, USA

## ABSTRACT

Principal slip surfaces in fault zones accommodate most of the displacement during earthquakes. The topography of these surfaces is integral to earthquake and fault mechanics, but is practically unknown at the scale of earthquake slip. We use new laser-based methods to map exposed fault surfaces over scales of 10  $\mu\text{m}$  to 120 m. These data provide the first quantitative evidence that fault-surface roughness evolves with increasing slip. Thousands of profiles ranging from 10  $\mu\text{m}$  to >100 m in length show that small-slip faults (slip <1 m) are rougher than large-slip faults (slip 10–100 m or more) parallel to the slip direction. Surfaces of small-slip faults have asperities over the entire range of observed scales, while large-slip fault surfaces are polished, with RMS values of <3 mm on profiles as long as 1–2 m. The large-slip surfaces show smooth, elongate, quasi-elliptical bumps that are meters long and as high as ~1 m. We infer that these bumps evolve during fault maturation. This difference in geometry implies that the nucleation, growth, and termination of earthquakes on evolved faults are fundamentally different than on new ones.

**Keywords:** faults, earthquakes, bumps, asperities, fault slip, slip surfaces, fault-surface roughness.

## INTRODUCTION

The amplitude and wavelength of bumps, or asperities, on fault surfaces affect all aspects of fault and earthquake mechanics, including rupture nucleation (Lay et al., 1982), termination (Aki, 1984), fault gouge generation (Power et al., 1988), lubrication (Brodsky and Kanamori, 2001), the near-fault stress field (Chester and Chester, 2000), resistance to shear, and critical slip distance (Scholz, 2002).

Despite its importance, knowledge of fault geometry and roughness is relatively limited at the scale of earthquake displacements. Prior comparative studies of natural fault roughness on multiple surfaces were based on contact profilometer data (Power et al., 1988; Power and Tullis, 1991; Lee and Bruhn, 1996). The method is labor intensive, so only a few profiles were reported for each surface. It was found that fault surfaces are smoother parallel to the slip direction than in the perpendicular direction and the fault surface relief is proportional to measured profile length (Power et al., 1988; Power and Tullis, 1991). Recent light detection and ranging (Lidar) measurements on one fault also suggested a power law relationship between protrusion height and profile length (Renard et al., 2006).

Here we investigate the relationship between slip-surface roughness and fault displacement using ground-based Lidar in the field and a laser profilometer in the laboratory. We cover a range of scales that includes the slip distances of observable earthquakes. By comparing geometrical features of different faults, we find that mature fault surfaces are smoother at small scales and have quasi-elliptical bumps and depressions at larger scales.

## SCANNED SURFACES AND SCANNING METHODS

Fault geometry is not trivial. Shear displacement can be carried by a single fault surface, by many, or by a zone depending on depth, lithology, and dynamics (Dor et al., 2006). Here we focus on the geometry of striated surfaces because they are a direct manifestation of localized shear, and continued displacement along them should affect their geometry. We chose nine faults that contain particularly well preserved slip surfaces with large (>5  $\text{m}^2$ ) exposures and few pits (Table 1; Fig. 1). Selecting coherent surfaces favors smooth surfaces overall, but does not bias the data to correlate smoothness with any other measured feature. The faults have prob-

ably been exhumed from the upper 5 km of the crust, and so they do not necessarily represent the earthquake nucleation region.

The Lidar (Leica HDS3000) measures precise distances over an area as large as hundreds of square meters with individual points spaced as close as 3 mm apart. The measured surface is combined with a digital photograph to discriminate the study areas from non-fault features (e.g., bushes, pits). We can then extract thousands of profiles in any direction (Fig. 2A). Each scan includes a portable planar reference sheet with a few square blocks of different known heights to constrain the noise level and resolution (Fig. 2B). Like the Lidar, the laboratory profilometer also produces a matrix of points. It covers a range of 10  $\mu\text{m}$  to 10 cm, allowing ~300–600 profiles on each hand sample.

The scan data are rotated so that the mean surface is parallel to a major axis and the mean striation direction is vertical or horizontal. The striation direction is established by finding the orientation that maximizes the cross correlation between adjacent profiles (Sagy et al., 2006). On each profile, spurious points with excessively large curvature (>4 standard deviations from the mean) were removed and data were interpolated across the gap. The data fraction removed is <3% in all cases.

To quantify fault roughness, we calculate the values of the root mean square (RMS) heights (average deviation of the topography from a planar surface) and the values of the power spectral densities (Power et al., 1988; Brown, 1995).

## RESULTS

Our data clearly indicate that net slip correlates with fault roughness. Small-slip faults (<1 m slip) are rougher (larger RMS values) than large-slip faults (~10–100 m slip) when measured parallel to the slip direction (Fig. 2).

For example, for 1 m profiles parallel to slip (along the axis of striations), the RMS height of the small-slip faults is  $6.5 \pm 3.5$  mm. For 2 m profiles, the RMS value is  $11.5 \text{ mm} \pm 5 \text{ mm}$  (Fig. 2A). The measured RMS heights of the large-slip faults we measured are so low that it is below the Lidar resolution limit for sections <3 m (Fig. 2A). Combining five scans of the same surface decreases the errors, and we find that the true

TABLE 1. SCANNED FAULTS

Fault name	Location	Displacement	Lithology	Sense
Split Mt. 1	33.014°N 116.112°W	30 ± 15 cm*	Sandstone	Strike slip
Split Mt. 2	33.0145°N 116.112°W	15 ± 5 cm*	Sandstone	Strike slip
Mecca Hills	33.605°N 115.918°W	20 ± 10 cm*	Fanglomerate (Calcite)	Strike slip
Near Little Rock	34.566°N 118.140°W	1–3 cm†§	Quartz diorite	Normal
Chimney Rock	39.227°N 110.514°W	8 m*	Limestone	Normal
River Mountains	36.062°N 114.831°W	500 m–1 km#	Dacite breccia	Normal
Flower Pit 1	42.077°N 121.856°W	100–300 m**	Andesite	Normal
Flower Pit 2	42.077°N 121.852°W	100–300 m**	Andesite	Normal
KF1	42.135°N 121.678°W	50–300 m**	Basalt + andesite	Normal
KF2	42.332°N 121.819°W	50–300 m**§	Basalt + andesite	Normal
Dixie Valley (The Mirrors)	39.795°N 118.075°W	>10 m††	Quartz	Normal

\*Direct measurements of offset of sedimentary layers or displacement of structural markers.

†Small-slip faults from within the Little Rock fault zone (not the main fault surface).

‡No large fresh outcrop exposures exist so only profilometer measurements were made.

§E.I. Smith, University of Nevada, Las Vegas, 2006, personal commun.

\*\*Belongs to the Klamath graben fault system in the northwestern Basin and Range (Personius et al., 2003). The faults are exposed by recent quarrying, so are relatively unweathered. Surfaces are on footwall Quaternary volcanic rocks (Fig. 1C) faulted against Holocene gravels. Minimum displacement along a single slip surface is >50 m. Assuming middle Pleistocene ages for the faulted volcanic rocks, and slip rates of 0.3 mm/yr (Bacon et al., 1999), the cumulative displacement is probably no more than a few hundred meters. The region is seismically active, including a 1993 sequence of earthquakes (Mw = 6).

††The fault is exposed in fine crystalline rocks (Fig. 1A). The fault zone includes several other anastomosing striated surfaces (see also Power and Tullis, 1992) in the ~10–20 m subjacent to the principal fault surface active in Quaternary time. The scanned surfaces probably formed at an unknown depth. The cumulative displacement along the fault zone may be 3 km or more, but individual slip surfaces probably accommodated smaller displacement.

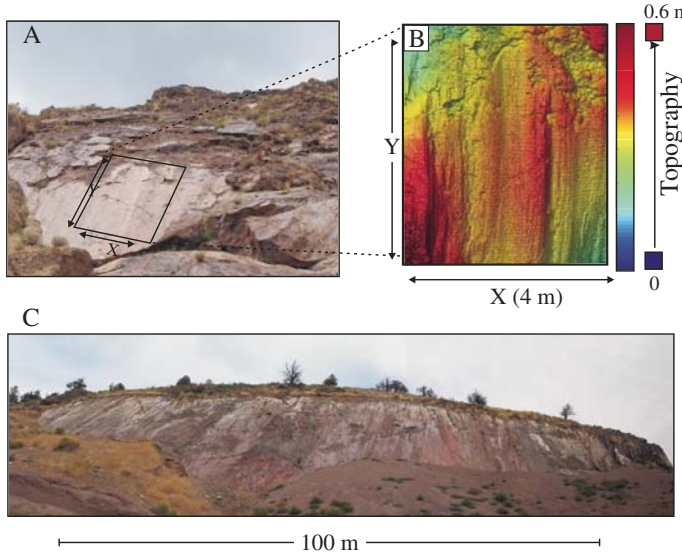


**Figure 1. Two of the large-slip fault surfaces analyzed in this paper.** A: Section of partly eroded slip surface at Mirrors locality on Dixie Valley fault, Nevada (Table 1). B: Light detection and ranging (Lidar) fault surface topography as color-scale map, rotated so that X-Y plane is best-fit plane to surface and mean striae are parallel to Y. C: One of three large, continuous fault segments at Flower Pit, Oregon (Table 1).

RMS is 3 mm for a 2 m profile of a large fault. These values are calculated from averaged detrended sections. Thus, at scales of 1–2 m parallel to the slip, the roughness of the large-slip faults is about one order of magnitude smoother than small-slip faults (Fig. 2).

Another measure of roughness is power spectral density. Fourier spectral analysis is a reliable indicator of roughness when based on many profiles (Simonsen et al., 1998). The spectral power is closely related to the RMS height of a profile. For example, for the special case of self-affine surfaces, the power spectral density  $p$  is related to the wavelength  $\lambda$  by

$$p = C\lambda^\beta, \quad (1)$$

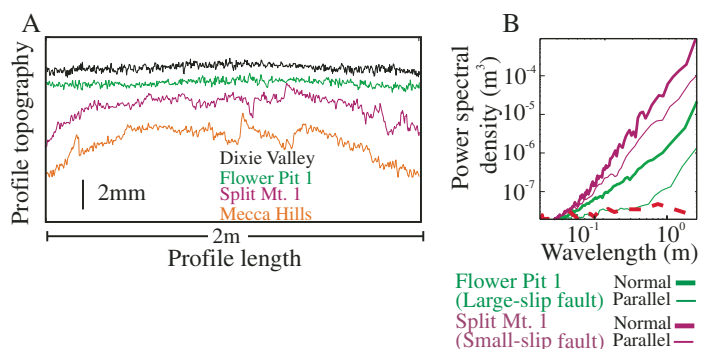


**Figure 2. Surface topography parallel and normal to slip orientation.** A: Profiles from four different fault surfaces parallel to slip direction. Upper two profiles are large-slip faults and bottom two profiles are small-slip faults. B: Power spectral density values for large-slip fault (green) and small-slip fault (magenta). Thick and thin curves are normal and parallel to slip, respectively. Each curve includes data from 200 individual 3 m profiles spaced 3 mm apart. Red dashed line represents scans of smooth, planar reference surface. Bending of power spectra at level of  $\sim 10^{-7.5}$  corresponds to resolution limit.

where  $C$  and  $\beta$  are constants (Brown and Scholz, 1985; Power and Tullis, 1991). If  $1 < \beta < 3$  for a section of length  $L$ , integrating equation 1 over wavelength  $\lambda$  yields the RMS roughness  $H$ :

$$H = [C/(\beta - 1)]^{0.5} L^{(\beta-1)/2}. \quad (2)$$

For simplicity, we describe one surface as rougher than another at a given wavelength if its power spectral density is higher at that wavelength (even when the surface is not necessarily self-affine).

Power spectral density curves from profiles parallel to slip extend the conclusions based on RMS roughness. Figure 2B shows an example of the results from one small-slip fault and one large-slip fault, for profiles both parallel and normal to striations. In each case, the spectra of 200 Lidar profiles separated by 3 mm and extending 3 m were computed with a multitaper method. The averaged result is presented only for wavelengths <1 m in order to avoid spurious finite length effects. The profiles parallel to slip are smoother (have lower spectral densities) than those normal to slip and large-slip faults are

smoother than small-slip faults. The difference between parallel and normal profiles is an obvious and expected consequence of striations, but the observed difference between large-slip and small-slip faults is novel to this study. Below wavelengths of  $\sim 0.5$  m, the power spectral density of the large-slip faults is nearly that of our smooth reference surface (red dotted line in Fig. 2B).

These results are supported by our full data set (Fig. 3A). Large-slip faults have consistently lower power spectral densities than small-slip faults. The difference in the two populations is clear in both the Lidar and laboratory data over scales from  $10\text{ }\mu\text{m}$  to 10 m.

The power spectral density results reflect the geometry for the large slip faults that can also be seen in topographic maps of the fault surface (Fig. 4). The three-dimensional (3D) Lidar data allow us to map lateral variability. At wavelengths  $>1$  m, the large-slip faults have undulating structures. At least three large-slip fault surfaces have smooth ellipsoidal ridges and depressions with dimensions that are  $\sim 1\text{--}5$  m wide,  $\sim 10\text{--}20$  m long, and  $\sim 0.5\text{--}2$  m high. The long axes of these bumps, or asperities, are parallel to the slip. Below  $\sim 1$  m wavelength, the Lidar data are limited by the instrumental noise.

The power spectra measured by the lab profilometer and field Lidar (Fig. 3A) for the large-slip faults do not easily connect across scales. One source of the discrepancy is that the surfaces are sufficiently smooth that the Lidar data are limited by noise at wavelengths  $<1$  m. A more subtle effect comes from joints. Examination of sections along the large faults suggests that most of the measured roughness in the Lidar scans at scales  $<1$  m is contributed by joints and small faults that cross the extremely smooth surface (Fig. 4A). Hand samples do not include these joints and therefore are smoother. The laboratory data suggest that the true fault-related roughness of the surfaces at scales of centimeters is likely much smaller than measured by the Lidar and may be consistent with the trend suggested by the laboratory data.

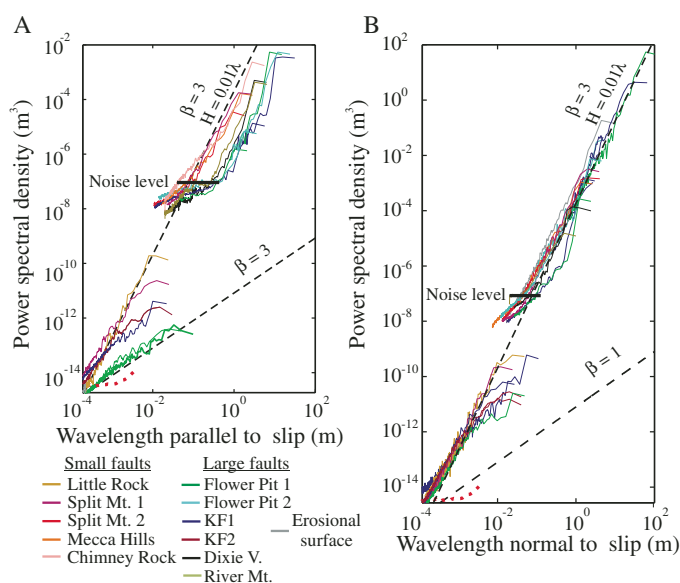


**Figure 3.** Power spectral density calculated from sections of seven different fault surfaces that have been scanned using ground-based Lidar (light detection and ranging), and from eight hand samples scanned by profilometer in lab. Each curve includes 200–600 continuous individual profiles from the best part of fault. Figure includes both Lidar data (upper curves) and laboratory profilometer data (lower curves) from profiles of a variety of lengths. A: Profiles parallel to slip. B: Profiles normal to slip. Red dashed line represent scans of smooth, planar reference surfaces for profilometer. Dashed black lines are slopes of  $\beta = 1$  and  $\beta = 3$ .

The slip-parallel profiles of large-slip fault surfaces are best described as polished on length scales  $\leq 1$  m and smoothly curved on larger scales (Fig. 4). The spectra show that the large-slip faults do not follow a power law. This behavior is in clear contrast to the former interpretation (Power and Tullis, 1991; Renard et al., 2006) and, combined with the differences between small-slip and large-slip faults, demonstrates that during slip faults evolve to geometrically simpler shapes.

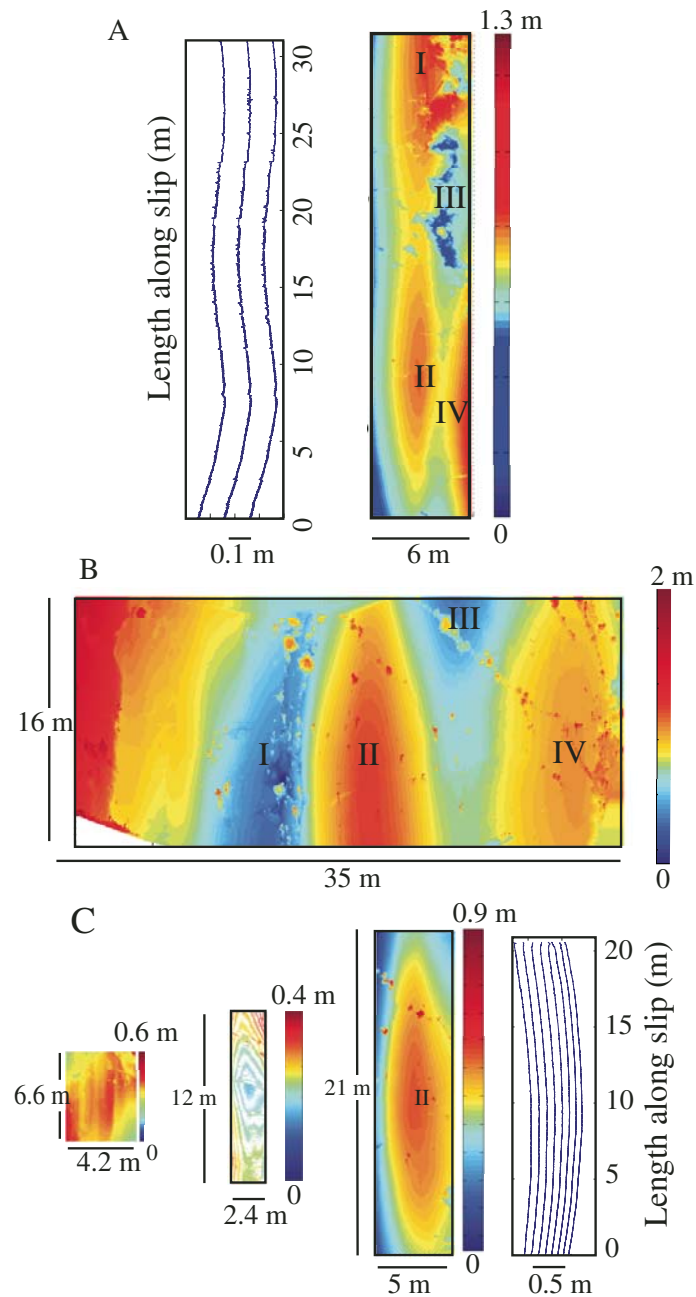


**Figure 4.** Fault surface topography of large scanned faults. A: Profiles (left) and map (right) of fault section (Klamath Falls 1). Map shows elliptical bulges (red) and depressions (blue) identical in their dimensions and aligned parallel to slip. Upper bulge (I) and depression (III) are partly eroded. B: Negative and positive elliptical bumps (marked by Roman numerals) on large section of fault surface (Flower Pit 1; see also Fig. 1C). C: Bumps on fault surfaces (Dixie Valley—left, Flower Pit 2—middle, Flower Pit 1—right). Right figure shows single elliptical bump and profiles along it. Middle image outlines single asperity with contours.

In the slip-normal direction, the data more nearly fit a power law (Fig. 3B). This observation supports and extends the results of previous studies (Power et al., 1988; Power and Tullis, 1991; Lee and Bruhn, 1996). The connection between the laboratory and field data is relatively simple for small-slip faults, as the power spectra measured by the lab profilometer and field Lidar follow a similar trend. This continuity across five orders of magnitude demonstrates the consistency of the two different measurement tools. The slopes of the power spectra of the large-slip and small-slip faults are similar, but the data fit the power law over different scales in each case. For example, one of the small faults (magenta in Fig. 3B) is fit with a power law that yields  $H = 0.015L^{0.98}$  from 10  $\mu\text{m}$  to at least 1 m (equation 2). The power spectral density of one of the large-slip faults (green in Fig. 3B) fits  $H = 0.009L^{0.94}$ . Although different analysis methods can be used to better calculate the exact slope  $\beta$  and its errors (Renard et al., 2006), the two examples suggest that roughness values follow the spectrum of a self-similar surface with  $H \approx 0.01L$  (upper dashed black line in Fig. 3B). Such a relationship has been observed for many natural faults and fractures (Brown and Scholz, 1985; Power and Tullis, 1991), and an arbitrary erosional surface has a similar spectrum (upper gray curve in Fig. 3B). We speculate that most of the slip-normal profiles reflect the roughness of natural fractures unmodified by slip. However, at least two of the large-slip faults fall significantly off this curve at scales  $< 1$  m (Fig. 3B). The physical structure behind this variation is the finite width of the bumps in Figure 4.

## DISCUSSION

The data presented are surprisingly consistent despite variations in lithology and fault type (Table 1). Because the large-slip faults are all normal faults in our data, at first it may appear that normal faults are systematically smoother than others. However, there is no obvious reason why normal faults should be smoother, but there are a number of physical reasons that slip should abrade faults. Therefore, we infer that displacement is the discriminating factor.

Smoothing of fault surfaces due to fault maturation may extend beyond outcrop scales. If the scale of the polished zones is slip dependent, then these zones should be much larger on faults that slip kilometers (Ben-Zion and Sammis, 2003). Our surface measurements complement previous map-scale observations of fault traces that suggested that the number of steps along strike-slip faults reduces with increasing displacement (Wesnousky, 1988).

Experiments, geological observations, and models also suggest that faults become geometrically simpler as they mature (Tchalenko, 1970; Chester et al., 1993; Ben-Zion and Sammis, 2003). Fracturing and abrasional wear are the most obvious mechanisms for smoothing fault surfaces. Tensile fracture surfaces typically follow a power law (Bouchaud et al., 1990), but wear preferentially eliminates small protrusions with slip. Thus wear is the more likely mechanism to produce the observed non-power law surfaces.

If the observed smoothness and regular elongated bumps are typical of mature faults at seismogenic depths and all other factors between faults are equal, then there are predictions for earthquakes that may be testable with modern seismic data. The mature faults should have more homogeneous stress fields and preferentially accumulate slip over geological time. High-frequency radiated energy should be less for mature faults than immature ones.

## CONCLUSION

We have shown through the variations in RMS roughness, spectral shape, and 3D geometry that faults evolve with slip toward geometrical simplicity. Slip surfaces of small-slip faults are relatively rough at all measured scales, whereas those of large-slip faults are polished at small scales but contain elongated quasi-elliptical bumps and depressions at scales of a few to several meters.

## ACKNOWLEDGMENTS

We thank R. Arrowsmith and Y. Ben-Zion for their reviews. We also thank J. Caskey, M. Doan, J. Fineberg, B. Flower, J. Gill, M. Jenks, B. Krantz, R. McKenzie, Z. Reches, S. Skinner, E. Smith, and A. Sylvester. Funding was provided in part by National Science Foundation grant EAR-0238455 and the Southern California Earthquake Center.

## REFERENCES CITED

- Aki, K., 1984, Asperities, barriers, characteristic earthquakes and strong motion prediction: *Journal of Geophysical Research*, v. 89, p. 5867–5872.
- Bacon, C.R., Lanphere, M.A., and Champion, D.E., 1999, Late Quaternary slip rate and seismic hazards of the West Klamath Lake fault zone near Crater Lake, Oregon Cascades: *Geology*, v. 27, p. 43–46, doi: 10.1130/0091-7613(1999)027<0043:LQSRAS>2.3.CO;2.
- Ben-Zion, Y., and Sammis, C.G., 2003, Characterization of fault zones: Pure and Applied Geophysics, v. 160, p. 677–715, doi: 10.1007/PL00012554.
- Bouchaud, E., Lapasset, G., and Planes, J., 1990, Fractal dimension of fractured surfaces—A universal value: *Europhysics Letters*, v. 13, p. 73–79.
- Brodsky, E.E., and Kanamori, H., 2001, Elastohydrodynamic lubrication of faults: *Journal of Geophysical Research*, v. 106, p. 16,357–16,374, doi: 10.1029/2001JB000430.
- Brown, S.R., 1995, Simple mathematical model of a rough fracture: *Journal of Geophysical Research*, v. 100, p. 5941–5952, doi: 10.1029/94JB03262.
- Brown, S.R., and Scholz, C.H., 1985, Broad bandwidth study of the topography of natural rock surfaces: *Journal of Geophysical Research*, v. 90, p. 2575–2582.
- Chester, F.M., and Chester, J.S., 2000, Stress and deformation along wavy frictional faults: *Journal of Geophysical Research*, v. 105, p. 23,421–23,430, doi: 10.1029/2000JB900241.
- Chester, F.M., Evans, J.P., and Biegel, R.L., 1993, Internal structure and weakening mechanisms of the San Andreas fault: *Journal of Geophysical Research*, v. 98, p. 771–786.
- Dor, O., Ben-Zion, Y., Rockwell, T.K., and Brune, J., 2006, Pulverized rocks in the Mojave section of the San Andreas Fault Zone: *Earth and Planetary Science Letters*, v. 245, p. 642–654, doi: 10.1016/j.epsl.2006.03.034.
- Lay, T., Kanamori, H., and Ruff, L., 1982, The asperity model and the nature of large subduction zone earthquakes: *Earthquake Prediction Research*, v. 1, p. 3–71.
- Lee, J.J., and Bruhn, R.L., 1996, Structural anisotropy of normal fault surfaces: *Journal of Structural Geology*, v. 18, p. 1043–1059, doi: 10.1016/0191-8141(96)00022-3.
- Personius, S.F., Dart, R.L., Bradley, L.A., and Haller, K.M., 2003, Map and data for Quaternary faults and folds in Oregon: U.S. Geological Survey Open-File Report 03-095, p. 550.
- Power, W.L., and Tullis, T.E., 1991, Euclidean and fractal models for the description of rock surface-roughness: *Journal of Geophysical Research*, v. 96, p. 415–424.
- Power, W.L., and Tullis, T.E., 1992, The contact between opposing fault surfaces at Dixie Valley, Nevada, and implications for fault mechanics: *Journal of Geophysical Research*, v. 97, p. 15,425–15,435.
- Power, W.L., Tullis, T.E., and Weeks, J.D., 1988, Roughness and wear during brittle faulting: *Journal of Geophysical Research*, v. 93, p. 15,268–15,278.
- Renard, F., Voisin, C., Marsan, D., and Schmittbuhl, J., 2006, High resolution 3D laser scanner measurements of a strike-slip fault quantify its morphological anisotropy at all scales: *Geophysical Research Letters*, v. 33, L04305, doi: 10.1029/2005GL025038.
- Sagy, A., Cohen, G., Reches, Z., and Fineberg, J., 2006, Dynamic fracture of granular material under quasi-static loading: *Geophysical Research Letters*, v. 111, B04406, doi: 10.1029/2005JB003948.
- Scholz, C.H., 2002, The mechanics of earthquakes and faulting: Cambridge, Cambridge University Press, 496 p.
- Simonsen, I., Hansen, A., and Nes, O.M., 1998, Determination of the Hurst exponent by use of wavelet transforms: *Physical Reviews E*, v. 58, p. 2779–2787.
- Tchalenko, J.S., 1970, Similarities between shear zones of different magnitudes: *Geological Society of America Bulletin*, v. 81, p. 1625–1640.
- Wesnousky, S.G., 1988, Seismological and structural evolution of strike-slip faults: *Nature*, v. 335, p. 340–342.

Manuscript received 25 July 2006

Revised manuscript received 9 November 2006

Manuscript accepted 20 November 2006

Printed in USA